Three-Dimensional Passive-Source Anisotropic Reverse Time Migration for Imaging Lithospheric Discontinuities: The Method

Peng Zou[1] **and Jiubing Cheng** [1]

[1]State Key Laboratory of Marine Geology, Tongji University, Shanghai, China.

Key Points:

- Seismic anisotropy in the receiver-side lithosphere has great impact on the scattered, teleseismic phases.
- Passive-source anisotropic reverse time migration can tackle strong heterogeneities and typical anisotropies.
- The symptoms of the split Ps phases in post-migration backazimuth domain reveal significance of appropriate treatments of the anisotropy.

Corresponding author: Jiubing Cheng, cjb1206@tongji.edu.cn

Abstract

The scattered teleseismic body waves have been used intensively to characterize the receiver-side lithospheric structures. The routinely used ray-therory-based methods have their own limitations to image complex structures and tackle strong heterogeneities. The newly developed wave-equation based, passive-source reverse time migration (RTM) approach can overcome such limitations, provided that multi-component seismograms have been recorded by regionally extensive seismic arrays of reasonable spatial sampling. To date, passive-source RTM has been developed only for isotropic media. However, at least to the first-order, most crustal and upper-mantle structures possess effective transverse isotropy with spatially variable symmetry direction. It is important to know how if we image the lithospheric discontinuities when seismic anisotropy is treated in an incorrect way. In this paper, we investigate the influence of elastic anisotropy on teleseismic P-to-S conversion at the lithospheric discontinuities and gain insights to explain why an isotropic RTM may fail to focus the converted wavefields from the perspective of relative arrival time variations with backazimuth and shear wave splitting. Accordingly, we extend the passive-source RTM approach for imaging three dimensional (3-D) lithospheric targets possessing transverse isotropy from the following two aspects: First, the teleseismic recordings with direct P and converted S phases are reverse-time extrapolated using rotated staggered grid (RSG) pseudo-spectral method which can tackle strong heterogeneity and transverse isotropies with symmetry axes in arbitrary direction; Second, the backward elastic wavefields are efficiently decomposed into vector anisotropic P and S modes to support accurate imaging. Two synthetic tests with hierarchical complexities reveal the significance of appropriate treatment of seismic anisotropy in passive-source RTM to characterize the receiver-side fine-scale lithospheric structures.

1 Introduction

In past decades, teleseismic body-wave scattering has been extensively used to characterize discontinuities in earth's crust, lithosphere-asthenosphere boundary, and mantle transition zone. The method commonly used has been the one of receiver functions (RFs), which were introduced and developed by Vinnik (1977) and Langston (1979). In this framework, essentially, the converted S-wave recording is deconvolved with the corresponding direct P-wave recording at each available station assuming a planarly layered earth model. Since then, various refinements have been developed for arrays of receivers. Common conversion point (CCP) stacking techniques are now routinely applied in the RF workflow to image interfaces in the

crust and mantle beneath the stations, e.g., Dueker & Sheehan (1997); L. Zhu (2000); Gao & Liu (2014). Stacking of multiple RFs over finite lateral and depth dimensions is necessary to enhance the signals of the converted waves as individual RFs often have low signal-to-noise ratios. Due to this spatial averaging, the CCP method can only produce good results for smoothly varying structures, and prevents accurate imaging of geologically complex structures, such as dipping and laterally discontinuous interfaces (e.g., strong interface topography, steep faults, steps in Moho). Moreover, stacking data from individual stations cannot adequately suppress scattering or diffraction hyperbola artefacts (L. Chen et al., 2005; Rondenay, 2009).

Several techniques have been presented to overcome the limitations of the conventional RF method. Ryberg & Weber (2000) demonstrated the application of Kirchoff poststack depth migration to synthetic data, and advocated that the concept of RF migration is theoretically sound. Revenaugh (1995), Levander et al. (2005), and C. Cheng et al. (2016) developed Kirchoff prestack depth migration to image scatters and velocity discontinuities. Bostock & Rondenay (1999) developed an inverse scattering approach for direct imaging of broadband array data using the theory developed by Beylkin (1985) for seismic reflection applications, which exploits an analogy between high-frequency, single scattering and the Radon transform. Poppeliers & Pavlis (2003) transformed the teleseismic recordings into ray-parameter and back-azimuth domain plane waves and migrated them separately. L. Chen et al. (2005) presented a wave-equation migration method, which back-propagates the CCP stacked RFs with an one-way phase screen propagator. Referring to a comprehensive theory of reverse-time migration (RTM) based inverse scattering in elastic media (Brytik et al., 2012), Shang et al. (2012) developed an elastic RTM approach to image crustal and mantle structures using teleseismic converted waves densely recorded by an array. Unlike the conventional RTM in exploration seismology (Baysal et al., 1983), which involves both source-side and receiver-side wavefields, this passive-source RTM approach requires only receiver-side backward propagated wavefield to form an image. Therefore, source related uncertainties, such as in epicenter location and origin time, are eliminated in teleseismic imaging of the structures beneath stations. By comparing the CCP and passive-source RTM results for a synthetic model with an offset in the Moho structure, Shang et al. (2012) demonstrated the advantages of this wave equation-based RF migration technique for complex structures. Compared to Kirchhoff migration, RTM is computationally more expensive, but has advantages to account for finite-frequency effects and overcomes, for example, multipathing in the propagating wavefield. Recently, Li et al. (2018) extended the passive-source RTM approach to 3-D spherical coordinate system, which may suit

for regional and global problems better. Note that all above studies focus on isotropic media, which limits their application to the lithospheric targets with evident seismic anisotropy, such as in subduction zone (Huang et al., 2011; Long & Wirth, 2013), orogenic belt(Xie et al., 2017) and beneath the cratons (Fouch & Rondenay, 2006).

Elastic anisotropy is the dependence of wave velocity on propagation direction. Generally, either orthorhombic or hexagonal symmetry is assumed when analyzing the earth. In most practice, people examine seismic anisotropy by analyzing variations of body-wave or surface-wave velocity in two orthogonal directions . The simplest model to explain these variations of velocity is hexagonal anisotropy or transverse isotropy (TI), although this probably average variations in other directions (Anderson & Regan, 1983; Savage, 1999). For instance, S-wave anisotropy of up to 4% is ubiquitous in the upper $200km$ of the lithosphere (Kaneshima et al., 1988; Savage, 1999). Anisotropy in the crust can be mainly caused by thin-bedded layering Backus (1962) and fluid-filled cracks (Crampin, 1984). In some areas (e.g. Tibet, Russian Urals, New Zealand), the lower crustal anisotropy may range up to 15%, mainly caused by highly anisotropic schists (Levin & Park, 1997). Upper mantle anisotropy is believed to result from strain-induced, preferred orientation of mantle minerals (mainly olivine). The sources to cause S-wave anisotropy also generate P-wave anisotropy with $5-9\%$ magnitude in the subducted slab and the largest crustal anisotropy (14%) related to schist (Eberhart-Phillips & Reyners, 2009; J. Wang & Zhao, 2012). Another important indicator of seismic anisotropy is shear wave splitting (SWS), in which the S-wave splits into two orthogonally polarized modes, each traveling with potentially different velocities (Christensen, 1966). To keep matters simple but capture the first-order features, seismologists usually explain the direction-dependence of P- and S-wave velocities and the behavior of shear wave splitting in terms of hexagonal anisotropy or TI, with vertical, horizontal or tilted symmetry axis (Anderson & Regan, 1983; Thomsen, 1986; Savage, 1999).

The passive-source RTM method use both direct P and converted S waves recorded by an array of stations to image the elastic discontinuities in the lithosphere. Its success relies on two key elements: an accurate reverse-time propagation of the elastic wavefields, and an imaging condition that can mitigate crosstalks among the wave modes and appropriately tackle shear wave splitting. It is important to know how if we use an isotropic migration algorithm while the subsurface medium is anisotropic. In this paper, apart from reviewing elastic body-wave propagation and polarization, we investigate the influence of elastic anisotropy on the teleseismic converted Ps phases, from the view of relative arrival time and shear wave splitting. Ac-

cordingly, we propose an anisotropic RTM method for imaging 3-D lithospheric targets. To tackle the hexagonal symmetries not aligned with the computational grids, we choose a rotated staggered-grid (RSG) pseudo-spectral scheme (Zou & Cheng, 2018) to reconstruct the subsurface elastic wavefields. High-fidelity and efficient wave mode decomposition (J. Cheng & Fomel, 2014) is used to precondition the reconstructed wavefields for accurately image the lithospheric discontinuities. Then, we show two synthetic examples to demonstrate the proposed approach in crustal extension and subduction zones. Finally, we discuss the ways to provide anisotropic velocity models and the possible alternative algorithms to reduce the computational cost for anisotropic RTM of teleseismic data.

2 Teleseismic Body-Waves in Anisotropic Lithosphere

2.1 Elastic body-wave propagation and polarization

For a linear elastic medium, the 3-D time-domain elastodynamic equation with source term is given by

$$\rho \partial_t u_i = \partial_j \tau_{ij} + f_i, \quad i = 1, 2, 3, \tag{1}$$

where $\rho = \rho(\mathbf{x})$ denotes density, $u_i = u_i(\mathbf{x}, t)$ are the particle velocities at a point $\mathbf{x}$ and time t, $\tau_{ij} = \tau_{ij}(\mathbf{x}, t)$ are the stress components and $f_i = f_i(\mathbf{x}, t)$ are the body-force components. We have used the Einstein summation convention over repeated indices, and a contracted notation for partial derivatives: $\partial_t \equiv \partial/\partial_t$, and $\partial_j \equiv \partial/\partial_{x_j}$. The stress and particle velocity components are related by the 3-D generalized Hooke's law through the stiffness tensor c_{ijkl} as follows:

$$\partial_t \tau_{ij} = c_{ijkl} \partial_l u_j. \tag{2}$$

Due to the inherent symmetries of stress and strain and the existence of a unique strain energy potential, only 21 elastic stiffness coefficients are independent, which usually simplified by Voigt notation (Auld, 1973) as c_{ij} (here, $i, j = 1, 2, 3, 4, 5, 6; j >= i$). The principal axes (called crystal axes in crystallography) are intrinsic axes, that define the symmetry of the medium. Most of the geological systems at different scales can be enough described by monoclinic, orthorhombic, hexagonal and isotropic media, which require 12, 9, 5, and 2 independent elasticity constants to fully describe the stress-strain relationship in the principal coordinate system, respectively.

Seismic waves are described by the elastodynamic equation with P- and S-waves intrinsically coupled. An anisotropic medium "splits" the S-wave into two modes with different ve-

locities. In the far-field, the polarization (or particle motion) vectors of the P-wave and the two S-waves are orthogonal, but in general not coincident with the dynamic axes defined by the propagation vector and plane of constant phase, thus we have the nomenclature of quasi-P (qP) and quasi-S (qS) waves. Substituting a plane-wave solution and the generalized Hooke's law into equation 1, neglecting the source term, gives the Christoffel equation:

$$(\widetilde{\mathbf{G}} - \rho {V_m}^2 \mathbf{I})\mathbf{a}_m = 0, \tag{3}$$

where $\widetilde{\mathbf{G}}$ represents the Christoffel tensor in the Voigt notation with $\widetilde{G}_{ij} = c_{ijkl} n_j n_l$, and n_j and n_l are the components of normalized propagation vector in the j- and l-th directions, with $i, j, k, l = 1, 2, 3$. The parameters V_m (m=qP, qS_1, qS_2), which associate with the three eigenvalues of Christoffel equation, represent phase velocities of qP, qS_1 (fast qS), qS_2 (slow qS) waves, respectively. The corresponding eigenvector $\mathbf{a}_m$ represents polarization direction of the given mode. If an eigenvalue coincides with one of the two remaining eigenvalues, the corresponding eigenvector cannot be uniquely determined. We then speak of the degenerate case. In realistic cases, the P-wave eigenvalue is well separated from the S-wave eigenvalues. This means that the degenerate case does not exist for P-waves. For S waves, however, there are two different degenerate cases (Crampin & Yedlin, 1981): (a) In anisotropic media, the two eigenvalues coincide locally along certain lines or at certain points on the slowness surface. We then speak of S-wave singularities and note that the polarization direction becomes a discontinuous function of phase direction. (b) In isotropic media, the two eigenvalues of S-wave coincide globally, and the polarization vectors can be in any two orthogonal transverse direction. In both these degenerate cases, the two S modes are coupled, locally or globally, and propagate as a single wave.

2.2 Hexagonal anisotropy in lithosphere

Although various mechanisms will lead to seismic anisotropy in the crust and upper mantle on a handful of scenarios, in many instances the effective anisotropy displays axis (i.e., hexagonal) symmetry to the first order (e.g. Thomsen, 1986; Savage, 1999). It can be caused by intrinsic anisotropy of the dominant mineral (e.g., mica, clay, serpentinite) or by periodic layering of materials with different elastic properties (Backus, 1962). Upper mantle anisotropy is most likely due to lattice preferred orientation (LPO) of olivine-rich rocks under dislocation creep (Mainprice et al., 2005). Foliated rocks such as gneisses and schists which believed to be the main cause of seismic anisotropy in the upper crust are orthorhombic or lower in symmetry. However, compilations of laboratory measurements of many laminated or foliated rocks

by Christensen (1966) and Godfrey et al. (2000) reveal that orthogonal measurements within the planes of foliation are similar (less than a few percent) particularly when compared with the measurement normal to the planes (several to > 10 percent). In these cases the approximation of hexagonal symmetry is valid.

Hexagonal symmetry requires five elastic constants in addition to the direction of the symmetry axis, and it is also called transverse isotropy (TI). When the symmetry axis is vertical, such anisotropy is called radial anisotropy or TI with a vertical symmetry axis (VTI). To separate the influence of the anisotropy from the 'isotropic' quantities chosen as the qP and qS velocities along the symmetry axis, Thomsen (1986) presented an alternative parameterization for VTI media:

$$v_{p0} = \sqrt{\frac{c_{33}}{\rho}}, \tag{4a}$$

$$v_{s0} = \sqrt{\frac{c_{44}}{\rho}}, \tag{4b}$$

$$\epsilon = \frac{c_{11} - c_{33}}{2c_{33}}, \tag{4c}$$

$$\delta = \frac{(c_{13} + c_{44})^2 - (c_{33} - c_{44})^2}{2c_{33}(c_{33} - c_{44})}, \tag{4d}$$

$$\gamma = \frac{c_{66} - c_{44}}{2c_{44}}, \tag{4e}$$

where v_{p0} and v_{s0} are the qP- and qS-wave velocities, respectively, along the symmetry axis. The parameter ϵ is controlled by the fractional difference between the vertical ($\sqrt{c_{33}/\rho}$) and horizontal ($\sqrt{c_{11}/\rho}$) P-wave velocities and is therefore analogous to the traditional measure of velocity anisotropy (Crampin, 1989). The parameter γ is an SH-wave version of ϵ. Although the definition of δ is less transparent than ϵ and γ, this parameter is responsible for the angular dependence of P and SV wave velocities, especially in the phase directions very close to the symmetry axis. We call ϵ as P-wave anisotropy, γ as S-wave anisotropy and δ as ellipticity (Becker et al., 2006). A useful advantage of this notation is that the dimensionless parameters, ϵ, δ and γ, collapse to zero in the case of isotropy. In general, two angles (dip angle α and strike angle ϕ) are required to specify an orientation of the symmetric axis, and the stiffness tensor in the Cartesian coordinate can be obtained through the Bond transformation from the principal coordinate frame. For the TI with a horizontal symmetry axis (HTI), Tsvankin (1997) introduced Thomsen parameters of the "equivalent" VTI model, which can be used to express the phase velocities and carry out seismic imaging.

2.3 The influence of anisotropy on teleseismic Ps phases

The analysis of scattered, teleseismic body waves to characterize the receiver-side lithosphere is now among the most widely used means of resolving fine-scale structure in these outer layers of the Earth. The lower mantle is generally assumed a smoothly varying and radial velocity structure. Therefore, the teleseismic wave propagation is relatively simple and can be effectively modeled by plane-wave sources over the breadth of the array. As the incident wavefield encounters discontinuities of elastic properties in the upper mantle and crust, it first generates forward scattered and converted waves that follow the incident waves to the surface. Then, the free-surface produces P and S reflections that further interact with underlying structure to produce backscattered energy recorded by the receiver array. Crustal reverberations are often considered a source of noise in lithospheric studies using the direct P and P-to-S conversions. Real data from epicentral distances less than 30° are complicated by triplications caused by upper mantle discontinuities, and data from epicentral distances larger than 90° are complicated by interaction with the core-mantle boundary. For passive-source RTM, we will focus on the forward P-to-S scatterrings in the lithosphere associated with the teleseismic P-wave at epicentral distance of $30^\circ < \Delta < 90^\circ$. In the isotropic case, an incoming plane P wave generates a single Ps phase at the discontinuity, whereas in the anisotropic case the converted S-wave generally splits into two orthogonally polarized modes, each traveling with different phase velocities and directions (Figure 1).

Ps receiver functions in hexagonal anisotropy media exhibit distinct azimuthal patterns, both on radial and transverse components. For instance, one can observe azimuthal amplitue variations on the radial component, polarity change on the transverse component and undulation of the delay time between direct P and converted Ps phases (Levin & Park, 1998). The time lag between the fast and slow modes of the split Ps phases is a quantitative indicator commonly used to constrain S-wave crustal anisotropy (e.g., McNamara & Owens, 1993; Liu & Niu, 2012).

For the RTM of teleseismic Ps phases, the key is applying an imaging condition to the decomposed P and S modes of the backward propagated elastic wavefields (Shang et al., 2012). In isotropic media, the divergence and curl operators are the traditional method for P/S separation. One can construct two-dimensional (2-D) anisotropic wave mode separation operators analogous to divergence and curl, based on the qP-qS polarization orthogonality (Dellinger, 1991). Fundamental complications occur with this method in three dimensions for shear waves,

because it is geometrically impossible to define a single global shear mode without discontinuities in polarization. Even weak orthorhombic anisotropy can cause the qS modes to split apart in a surprising way and the qS_1 and qS_2 modes are not individually continuous. This problem is not insurmountable; the isotropic separation into P, SV and SH waves enjoys wide use despite the discontinuity for vertically propagating S-waves. Similar separations are useful for TI media, because the qS-waves can be designated as qSV and qSH modes with globally continuous polarizations, except in the degenerate direction along the symmetry axis (Dellinger, 1991; Yan & Sava, 2009). The SH-wave always polarizes in the isotropy plane as a pure mode and the qSV-wave always polarizes in the plane formed by the symmetry axis and the propagation direction. Therefore, in this study, the influence of seismic anisotropy on RTM of the Ps phases will be investigated from the view of relative arrival times between the direct qP phase and the converted qSV and qSH phases. For simplicity, we will not strictly distinguish the nomenclature P, SV and SH with qP, qSV and qSH in the following sections.

A hexagonal medium has a single axis of rotational symmetry. Therefore, all seismic signatures depend just on phase angle, i.e., the angle between the symmetry axis and propagation direction. In the weak-anisotropy approximation, Thomsen (1986) derived a linearized formulation of the phase velocities for the three wave modes:

$$v_p(\theta) = v_{p0}(1 + \delta \sin^2\theta \cos^2\theta + \epsilon \sin^4\theta), \tag{5a}$$

$$v_{sv}(\theta) = v_{s0}\left[1 + \frac{v_{p0}^2}{v_{s0}^2}(\epsilon - \delta)\sin^2\theta\cos^2\theta\right], \tag{5b}$$

$$v_{sh}(\theta) = v_{s0}(1 + \gamma \sin^2\theta), \tag{5c}$$

where θ is the phase angle. Accordingly, we can evaluate the influence of hexagonal anisotropy on the propagation and imaging of the teleseismic data. For a given planar P-wave incidence with horizontal slowness p and backazimuth Φ, the relative arrival times of the converted qSV and qSH phases associated with a lithospheric interface at the depth of H below a homogeneous and anisotropic layer (Figure 1b) can be respectively expressed as:

$$T_{p-sv}(p,\Phi) = H\left[\sqrt{\frac{1}{v_{sv}^2(\theta_{sv}(p,\Phi))} - p^2} - \sqrt{\frac{1}{v_p^2(\theta_p(p,\Phi))} - p^2}\right], \tag{6}$$

and

$$T_{p-sh}(p,\Phi) = H\left[\sqrt{\frac{1}{v_{sh}^2(\theta_{sh}(p,\Phi))} - p^2} - \sqrt{\frac{1}{v_p^2(\theta_p(p,\Phi))} - p^2}\right], \tag{7}$$

with θ_p, θ_{sv} and θ_{sh} representing phase angles of the transmitted qP, qSV and qSH waves, respectively. Given the medium parameters and the incident direction defined by p and Φ, one can calculate the phase angles using the Snell's law.

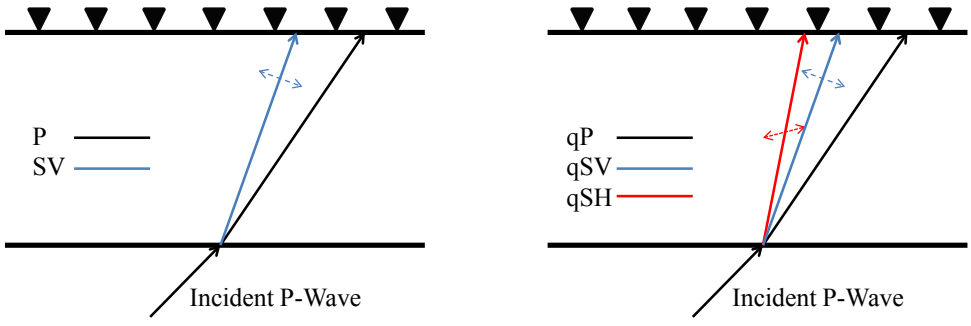

(a) (b)

Figure 1: A schematic diagram illustrating raypaths of teleseismic body-waves in the localized zone below the array. A planar P-wave from a distant earthquake travels through an isotropic layer (a) or a transversely isotropic layer (b) before being recorded by the stations (black triangles). The solid lines denote wave propagation direction of each wave mode, and the thin dash lines indicate polarization directions of S-waves. In the presence of anisotropy, the converted Ps wave splits into two orthogonally polarized modes, which can be designated as qSV and qSH waves in the process of wavefield propagation.

We illustrate the relative arrival times of the Ps phases on a crustal extension model, in which the depth of Moho is $33km$ and the crustal anisotropy results from predominately granite with fluid-filled cracks, e.g., Jones et al. (1999). The stiffness tensor was calculated assuming an isotropic granitic host rock with P-wave velocity of $6.5km/s$, S-wave velocity of $3.8km/s$ and a density of $2.6g/cm^3$. The effects of vertical fluid-filled cracks were modelled using the self-consistent scheme (SCM) (Nishizawa, 1982). Cracks in the crust have an aspect ratio of 0.06 and the host rock has a crack porosity of 5 percent (resulting in a crack density of 20 percent). The coefficients of crack orientation distribution function (CODF) were chosen so that the crustal layer possesses HTI symmetry, of which the Thomsen parameters of the equivalent VTI model is given by $\epsilon = -0.08, \gamma = -0.06$ and $\delta = -0.16$. In addition, the elasticity of the isotropic mantle material is defined with P-wave velocity of $7.8km/s$, S-wave velocity of $4.6km/s$ and a density of $3.0g/cm^3$, respectively. Figure 2 displays variations of the relative arrival times for qP-qSV, qP-qSH phases and an isotropic converted phase for refer-

ence. We observe that both T_{p-sv} and T_{p-sh} vary with backazimuth, and the former has greater variations. In this example, the largest deviation from the isotropic counterpart approaches $0.5s$, which means a depth shift of about $5.0km$ if neglecting the anisotropy.

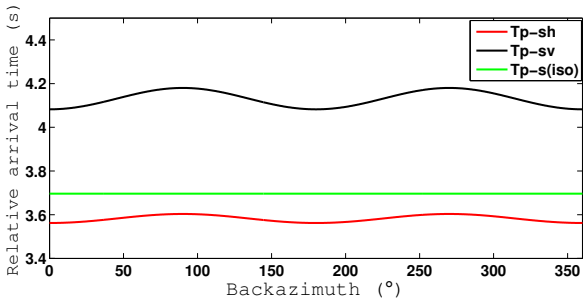

Figure 2: The relative arrival times of qP-qSV, qP-qSH and their isotropic counterpart associated with backazimuth of an incident planar P-wave with a horizontal slowness of $0.053s/km$ in a crustal extension model.

We further check the waveforms of the converted Ps phases in the synthetic three-component (3C) seismograms for the crustal extension model. As shown in Figure 3a, a regular station network is deployed on the surface of the model, of which the size is $80km \times 80km \times 60km$ in three dimension. Plane-wave sources with horizontal slowness between $0.040s/km$ and $0.077s/km$ are used to mimic the teleseismic sources at $30^\circ \sim 90^\circ$ epicentral distance. We record 3C particle velocity with the stations in a recording time of $20s$. These synthetic seismograms will be used as "data" for the first RTM experiment in the example section. Figure 3b shows a 3C seismogram recorded by one of the station for a planar P-wave incidence. We can observe the split Ps phases on the two horizontal components, of which the x-component is dominated by the P-to-SV conversion and the y-component dominated by the P-to-SH conversion, with a time lag of about $0.5s$. This essentially agrees with the analytic estimate of their kinematics using the phase velocity formulations (Figure 2).

3 passive-source Reverse Time Migration in Anisotropic Lithosphere

Deployments of regionally extensive seismic arrays of reasonable spatial sampling yield teleseismic data amenable to array-based processing (e.g., RTM) for delineating receiver-side small-scale heterogeneities in the crust and upper mantle. In general, passive-source RTM mainly consists of three steps (Shang et al., 2012; Li et al., 2018): First, back-propagated elastic wave-fields in subsurface are reconstructed through reverse-time extrapolating the multi-component

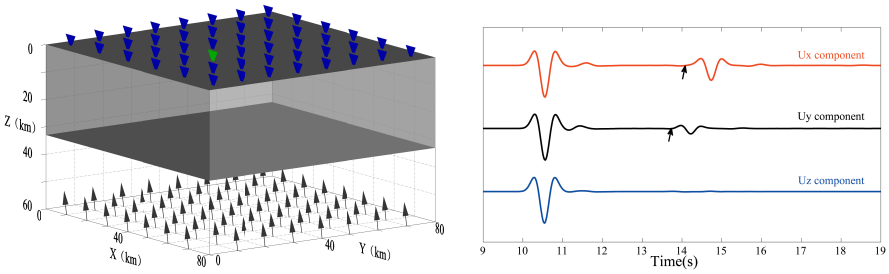

(a) (b)

Figure 3: Synthetic teleseismic recordings on the 3-D crustal extension model: (a) Sketch map of the station network (denoted by triangles) and the model geometry beneath the recording network. (b) 3C seismograms recorded by a station (denoted by green triangle) for a planar P-wave incidence with a backazimuth of 135° (due north) and incidence angle of 25° (from the vertical). The relative arrival times of the converted S phases are picked on $x-$ and $y-$components of the seismograms.

seismograms. Then, P/S separation of the elastic wavefields is carried out at each time-step to mitigate crosstalks between the two wave modes. Finally, an appropriate imaging condition is applied to the decoupled P and S fields to yield an image of the elastic discontinuity. Stacking amounts of images of the selected earthquakes improves the quality of final result. In this procedure, both wavefield extrapolation and mode decomposition can be affected by P- and S-wave anisotropies in the crust and upper mantle. In the subduction zone, orogenic belt or near the periphery of the craton, depth-dependent tilted hexagonally symmetry is very common (Long & Wirth, 2013; Xie et al., 2017). To adapt anisotropic symmetries in the lithosphere not aligned with the computational grids, we will first review a pseudo-spectral method that can simulate elastic wave propagation in 3-D arbitrary anisotropic media. Then we will present a vector-product imaging condition based on an efficient mode decomposition of the elastic wavefields in heterogeneous TI media with the polarization projection.

3.1 Pseudo-spectral method for anisotropic wavefield extrapolation

Among the most popular numerical methods for simulating seismic wave propagation, we choose pseudo-spectral method (PSM) using rotated staggered grids (RSG) (Zou & Cheng, 2018) as a solver of the first-order elastic wave equations in 3-D anisotropic media due to the three factors: First, the PSM can save computational memory and time because the spectral

operators permit larger grid spacing to calculate the spatial derivatives (Kosloff & Baysal, 1982). Second, when the symmetry axis of a TI medium is not aligned with the computational grid, a straightforward use of the standard staggered grids (SSG) is problematic because of essentially different and complicated representations of Hooke's law. The RSG configuration makes the PSM applicable to 3-D arbitrary anisotropic media and at the same time avoids any cumbersome interpolation operation such as in the SSG implementation (Zou & Cheng, 2018), because three particle velocity components with all the stiffness coefficients are defined at the same location and all stress components are placed at the center of the grid cells (Saenger & Bohlen, 2004). Third, the particle velocity components calculated by the RSG-based PSM can be directly used for wave mode decomposition because all of them are defined at the same nodes and thus don't require any adjustments as in the SSG-based schemes, e.g., Zhang & McMechan (2010).

Grid staggering is essential for a PSM to suppress the non-causal ringing artifacts in simulating seismic wave propagation, but the standard implementation can only be used to model anisotropy up to orthorhombic media and the symmetry axis aligned with the computational grid. In RSG-based PSM, the spatial derivatives in equations (1) and (2) can be calculated by the following discrete formula:

$$D_j^{\pm}\varphi = \sum_{k_j=0}^{k_j(N)} ik_j \cdot s^{\pm} \cdot \tilde{\varphi}(k_j) e^{ik_j j}, \tag{8}$$

with

$$s^{\pm} = e^{\pm i(k_x \Delta x/2 + k_y \Delta y/2 + k_z \Delta z/2)}, \tag{9}$$

in which k_j $(j = x, y, z)$ denotes the wavenumber with respect to one of the coordinates, and $k_j(N)$ represents the corresponding Nyquist wavenumber, s^+ or s^- is a forward or backward phase shift to amend the staggered differential operator, i is an imaginary unit, $\tilde{\varphi}$ denotes the Fourier transform of φ. With these spectral derivative operators, the elastodynamic equation and stress-strain equation can be solved by using

$$\rho \partial_t u_i = D_j^{+} \tau_{ij} + f_i, \tag{10}$$

and

$$\partial_t \tau_{ij} = c_{ijkl} D_l^{-} u_k. \tag{11}$$

The equation of motion only involves forward-shifted spectral derivative operators, whereas the constitutive relation only involves backward-shifted spectral derivative operators. This implies that all the phase shifts can be merged into the spectral derivative operations, and thus no extra fast Fourier transformation is required. This RSG-based PSM provides a good solu-

tion for simulating 3-D elastic wave propagation in a TI medium with strong heterogeneities and arbitrary variations in the direction of the symmetry axis. More details can be found in Zou & Cheng (2018).

3.2 Imaging based on wave mode vector decomposition

In elastic RTM, for whether active- or passive-source seismic data, decoupling the wave modes in the far-field is a prerequisite for imaging to get physically interpretable results with fewer crosstalks (Shang et al., 2012; C. Wang et al., 2016). In general, for the well-behaved qP mode, the wave polarization $\mathbf{a}_p$ can be determined by solving the Christoffel equation (3). Therefore, Dellinger (1991) proposed an approach to separate qP and non-qP (qS) fields based on polarization projection only involving the polarization direction of qP-wave ($\mathbf{a}_p$). However, the polarization directions of the two qS modes cannot be consistently determined in this way because of the S-wave singularities (Crampin & Yedlin, 1981). So it is not wise to separate qS_1 and qS_2 in the extrapolated wavefields for the imaging purpose. To our interest, in TI media, the qS-waves can be designated as qSV and qSH modes with globally continuous polarizations, except in the degenerate direction along the symmetry axis. The far-field qP, qSV and qSH waves in the same propagation direction possess polarization orthogonality, which provides theoretical cornerstone to decouple them in the plane-wave domain during wavefield extrapolation. Accordingly, Yan & Sava (2009) suggested to further decouple the qS field into qSV and qSH modes based on the qP-qSV-qSH polarization orthogonality in TI media. To honor vector fidelity, the far-field elastic wavefield at any moment can be decomposed through (Zhang & McMechan, 2010):

$$\mathbf{U}_m(\mathbf{k}) = \bar{\mathbf{a}}_m(\mathbf{k})[\bar{\mathbf{a}}_m(\mathbf{k}) \cdot \mathbf{U}(\mathbf{k})], \tag{12}$$

where $\bar{\mathbf{a}}_m$ ($m = qP, qSV, qSH$) represents the normalized polarization vector in the phase direction $\mathbf{k}$, and $\mathbf{U}$ is the vector wavefield of particle velocity in wavenumber-domain. This mode decomposition preserves the origional physical units, phases, particle motion amplitudes and directions. To tackle spatial heterogeneities of the anisotropic media, the equation (12) can be extended to a generalized Fourier integral operator (J. Cheng & Fomel, 2014):

$$\mathbf{u}_m(\mathbf{x}) = \int e^{i\mathbf{k}\mathbf{x}} \bar{\mathbf{a}}_m(\mathbf{x}, \mathbf{k})[\bar{\mathbf{a}}_m(\mathbf{x}, \mathbf{k}) \cdot \mathbf{U}(\mathbf{k})] d\mathbf{k}. \tag{13}$$

In passive-source RTM, separation of qP and qS fields is sufficient for the imaging condition to characterize the lithospheric discontinuities. In this case, equation 13 is only used for isolating qP vector field, and the qS vector fields can be directly obtained, i.e., $\mathbf{u}_{qS}(\mathbf{x}) = \mathbf{u}(\mathbf{x}) - \mathbf{u}_{qP}(\mathbf{x})$. Further separation of qSV and qSH modes is helpful for investigating the effects of

anisotropy (e.g., S-wave splitting and azimuthal signatures) on the RTM images. For TI media with spatial heterogeneities, the above integral operator is equivalent to a nonstationary filtering. The computation complexity of the straight-forward implementation is $O(N^2)$, which is prohibitively expensive when the size of model N is large. We apply a model-adaptive low-rank approximation to the mixed-domain integral kernels in equation 13 (J. Cheng & Fomel, 2014) to reduce the computation complexity to $O(rN \log N)$, and the rank r is very small and usually below the order of tens.

To take full advantage of the vector information (e.g. polarization and polarity) of the separated qP and qS wavefields, we prefer to applying the imaging condition proposed by C. Wang et al. (2016) in exploration seismology to the RTM of teleseismic data. Thus the vectorial cross-correlation of the separated wavefields

$$I_{ps}(\mathbf{x}) = \sum_{n=1}^{n_s} \frac{w_n}{|\kappa_n|} \int_0^T [\mathbf{u}_{qP}(\mathbf{x}, t) \cdot \mathbf{u}_{qS}(\mathbf{x}, t)]_n dt, \tag{14}$$

is used to image the elastic discontinuities that cause the qP-to-qS mode conversion for n_s selected earthquakes within the required epicentral distance. The scale factor

$$\kappa_n = \int_0^T [\bar{\mathbf{a}}_p(\mathbf{x}, t) \cdot \bar{\mathbf{a}}_s(\mathbf{x}, t)]_n dt, \tag{15}$$

is applied to balance the image amplitudes, and the weight w_n can be determined according to the image quality of an individual event (such as signal-to-noise ratio). We can obtain two more images by vectorial cross-correlation of the separated qP and qSV (or qP and qSH) fields for interpretive use. Note that, this vector imaging condition automatically avoids the polarity-reversal issue that often damages the elastic RTM based on conventional imaging condition, and maintains a consistent polarity for a given elastic contrast (C. Wang et al., 2016).

3-D RTM is a computationally heavy task and the cost is generally proportional to the number of earthquakes used in imaging. For passive-source RTM in isotropic media, Li et al. (2018) adopted a parallel algorithm on high-performance cluster of multi-core CPUs. The computational demands tremendously increase in 3-D anisotropic media because more partial derivatives related to none-zero stiffness coefficients are required to extrapolate the wavefields. For TI media with strong spatial heterogeneities, it still takes a large amount of time to decompose the elastic wavefields into pure mode fields, even though the low-rank approximate algorithm has been used. To make the proposed 3-D anisotropic RTM computationally affordable, our solution is to leverage the massively parallel architecture of graphic processing units (GPUs) to accelerate the computation in wavefield extrapolation and mode decomposition.

391 ## 4 Numerical Examples

392 In this section, we will test the approach and investigate how anisotropy influences the
393 RTM results of the lithospheric discontinuities with two synthetic data sets. We first explore
394 how the image of the Moho may be biased if seismic data acquired over a transversely isotropic
395 crustal layer are imaged with inaccurate Thomsen parameters or assuming isotropy. Then we
396 investigate what gains can been made by passive-source anisotropic RTM in the subduction
397 zone possessing realistic transverse isotropies with varied symmetry axes in different layers.
398 These numerical experiments are implemented on a workstation with four NVIDIA RTX 2080
399 Ti GPU cards.

400 ### 4.1 Crustal extension model

401 We first study the effects of crustal anisotropy and consider a single HTI layer overly-
402 ing an isotropic elastic half-space. The 3D-3C seismograms synthesized by using the RSG-
403 based PSM in the previous section are processed with the passive-source RTM algorithm. For
404 the 120 events, the incident angles at the Moho vary from 15° to 25° in 2° increments, while
405 the back-azimuths vary from 0° to 360° in 15° increments. For simplicity, we employ Ricker
406 wavelet with central frequency of $1.0Hz$ as the source time function. This simplification is
407 justifiable as a source-equalization and deconvolution step can be applied to real teleseismic
408 data to remove the source effects, e.g., Rondenay (2009). In order to investigate the influence
409 of anisotropy, we respectively carry out four experiments with: (a) the true anisotropic model;
410 (b) an inaccurate anisotropic model by setting $\epsilon = 0$; (c) an inaccurate anisotropic model by
411 setting $\gamma = 0$; (d) an isotropic model by setting $\epsilon = 0$, $\gamma = 0$ and $\delta = 0$. We do not check
412 the impact of δ because it only influences the wave propagation around the symmetry axis of
413 the HTI layer and thus has few effect on the teleseismic phases to our interests in this exper-
414 iment.

415 Both wavefield extrapolation and P/S mode decomposition are based on the given mi-
416 gration velocity models. Figure 4 displays the RTM images and common image gathers (CIGs)
417 in the backazimuth domain with these models. We observe that correct imaging depth and high
418 signal-to-noise ratio can only be guaranteed with the true anisotropic model. Remarkable resid-
419 ual moveouts varied with the backazimuths lead to inaccurate RTM images and artifacts re-
420 sulting from mode crosstalks and unfocused wavefields, when the inaccurate migration veloc-
421 ity models are used. To further explain the imaging results, we decompose the S wavefields

into SV and SH modes, and output the CIGs of the P-SV and P-SH converted phases. Along with the time-to-depth conversion according to equations (6 and 7), these CIGs provide insightful clues to reveal the influence of the anisotropic parameters (Figures 4 and 5). Energy gaps on the P-SV and P-SH CIGs are clearly observed because there are no P-to-SV (or P-to-SH) conversion when the elastic waves propagate perpendicular to (or parallel with) the symmetry axis of the HTI media. These CIGs indicate patterns of amplitude variations with the backazimuths for P-SV and P-SH phases. Weak P-to-SH conversion at this interface causes relatively small amplitudes on the P-SH CIGs. Neglecting the P-wave anisotropy by setting $\epsilon = 0$, P-SV and P-SH CIGs display almost consistent residual moveouts in the backazimuth domain, and eventually lead to about $5km$ misfit between the stacked image of the Moho and its true depth, see Figures 4c, 5d, 5e and 5f. As shown in the last two rows in Figure 4, neglecting the S-wave anisotropy leads to severly distorted images for the Moho in the backazimuth domain, and two split interfaces in the stacked images. For the corresponding P-SV and P-SH CIGs in Figure 5, we see that accurate P-wave anisotropy guarantees correct imaging depths for the P-SV conversion at various backazimuths, whereas inappropriate treatments of S-wave anisotropy result in back-propagation of the split S-wave fields with incorrect phase velocities and sever mode leakage in the P-SH images at most backazimuths. As shown in Figures 5g and 5i, the P-SH conversions nearly all are imaged at shallower depths for various backazimuths. When we use an isotropic velocity model by setting ϵ, γ and δ as zeros, the P-SV conversions all focused at much deeper locations while the P-SH conversions are focused at slightly shallower locations for various backazimuths. In this case, the depth errors of the P-SH images are relatively small because the phase velocities of P and SH modes have similar changing trends when assuming isotropy (equation 5). For the split images of the Moho in Figures 5i and 5l, the upper flattened events are the contribution of P-SV conversions while the lower bending events mainly result from the leaked P-SV energy due to inappropriate treatments of S-wave splitting. The NVIDIA RTX 2080 Ti GPU has a large amount of computational units but limited memory resource (only 12GB per card), so we need to use RSG-based PSM for allowing large grid spacing for 3-D wavefield extrapolation. Thanks to the powerful computational capability, it takes half an hour to finish the RTM task of all 120 earthquakes with four these GPU cards.

4.2 Subduction model

Then we demonstrate the passive-source anisotropic RTM approach with a synthetic teleseismic data on a subduction model, which is summarized and simplified from the Hikurangi subduction zone (Eberhart-Phillips & Reyners, 2009) and northeast Japan subduction zone (Huang et al., 2011). It contains an isotropic layer in the crust, trench-normal (HTI) anisotropy of 6% and 2% for P- and S-waves in the mantle wedge, and trench-parallel (tilted TI) anisotropy of 8% and 2% for P- and S-waves in the intra subducting slab, respectively. For calculation purposes, we take it as a multi-layer VTI model with the equivalent Thomsen parameters. We assume that there exists no lateral variation along the y direction and ignore the subslab anisotropy for simplicity. Figure 6a displays the subduction structures with the vertical P-wave velocities in the section perpendicular to the slab, while the vertical S-wave velocities are given by a constant Vp/Vs ratio. We have synthesized the scattered Ps phases for 24 teleseismic P-wave incidences to illuminate the subduction zone, of which the incidence angles vary from 15° to 21° with an uniform increment of 3.5° and the backazimuths vary from 5° to 360° with an uniform increment of 30°. The anisotropic models are preconditioned through gaussian smoothing with a radius of $8.0km$ for RTM.

We observe remarkable differences between the RTM results with and without taking into account anisotropy. In the anisotropic RTM image (Figure 6b), the main peaks of the events match well with the elastic discontinuities of the true models and yield good constraints on the subduction structures. Neglecting the anisotropy, the RTM algorithm results in a problematic image for the subducting slab (Figure 6c): First, the top boundary is gradually smeared and eventually split into two events with strong positive polarities, while the bottom boundary is servely smeared and represented by two unfocused events with negative polarities as the mantle wedge becomes thick. Second, the maximum deviation of the slab depths exceed $5.0km$ beneath the thick anisotropic layers. Third, the signal-to-noise ratio descends due to unfocusing of the back-propagated energy and insufficient P/S mode decoupling when assuming isotropy. The CIGs further reveal that the anisotropic RTM guarantees correct imaging depths for all backazimuths, whereas the isotropic RTM causes wrong imaging depths and fails to focus the split S-wave fields (Figure 7).

5 Discussion

The success of the proposed approach to image the 3-D anisotropic lithosphere relies on the following conditions: a dense multicomponent seismic network, high-performance computation, and appropriate anisotropic velocity models. Li et al. (2018) and Jiang et al. (2019) have investigated the spatial sampling requirements on the surface for RTM and pointed out that the distance between two stations should be in the range of 5-10 km for a typical maximum frequency of 1.0 Hz of the teleseismic RFs. The GPU-based wavefield extrapolation and mode decomposition makes passive-source RTM computationally affordable for regional seismological studies. In presence of strong heterogeneity and anisotropy, the polarization-based mode decomposition is still a computational burden even though we have resorted to the low-rank approximation algorithm. A possible approximate solution to avoid separating the P and S fields is to isolate the direct P and its coda and then respectively back-propagate with smooth anisotropic velocity models. A further simplification may be to back-propagate the separated P and Ps phases with pure-mode propagators of qP and qS waves which honor the wavefield kinematics, e.g., J. Cheng & Kang (2014, 2016).

Accurate models of P- and S-wave velocities are essential for RTM of the teleseismic Ps phases to produce reliable structural images. For many years the most widely used 1-D model of the Earth's seismic velocities has been the Preliminary Reference Earth Model (PREM) (Dziewonski & Anderson, 1981). The updated crust and lithosphere models, CRUST1.0 (Laske et al., 2013) and its extension LITHO1.0 (Pasyanos et al., 2014) delineate elastic properties of multi-layer sediment and crust with nominal resolution to 1°, constrained by many different datasets, including extremely large datasets of relatively short-period velocity measurements and compilations of receiver function constraints and active source seismic studies. They provide P- and S-wave velocities for 3-D RTM if the subsurface structures are relatively simple or there is no finer model available in the studied region. The parameters describing P- and S-wave anisotropies and the direction of the symmetry axis are also required to image the lithospheric structures with TI symmetry. Shear wave splitting measurements (e.g., Yuan & Beghein (2013); Rumpker et al. (2014)) and anisotropy-aware RF analyses (e.g., Levin & Park (1997); Eckhardt & Rabbel (2011)) can provide constraints to these parameters of the crust and upper mantle. The rapid growth in global seismic instrumentation, combined with the implementation of automated methods, have enabled the generation of a variety of global, continental-scale anisotropic tomography models, e.g., Lebedev & Hilst (2008); Yuan & Beghein (2013); Chang et al. (2015); Schaeffer et al. (2016) and see Zhao et al. (2016) for a review. With the recent

emergence of large-scale dense arrays of broad-band instruments, the mapping of the 3-D distribution of velocity and anisotropy has been performed with increasingly higher resolution, for instance using adjoint tomography e.g., M. Chen et al. (2015); H. Zhu et al. (2020), now approaching the accuracy required for passive-source RTM to improve the lithospheric imaging. Theoretically, full waveform inversion (FWI, Tarantola, 1984) has the potential to dramatically improve the resolution of tomographic models due to the exploitation of both the amplitude and phase of seismic waves. However, the real data application of anisotropic FWI still an important challenge and needs substantial efforts (Beller & Chevrot, 2020).

6 Conclusions

To characterize the fine-scale structures in the anisotropic crust and upper mantle with the scattered teleseismic data, we have proposed an array-based passive-source 3-D elastic RTM approach that honors the azimuthal variations of the relative arrival times of the converted Ps phases and the presence of shear wave splitting. Compared with the isotropic counterpart, it has the following differences and improvements: First, elastic wavefield backward propagation using the 3-D RSG-based PSM and polarization-based vector decomposition of qP and qS fields support accurate imaging in heterogeneous media with vertical, horizontal and tilted hexagonal symmetries. Second, low-rank approximate polarization projection and GPU-based acceleration make the 3-D anisotropic RTM algorithm computationally affordable. The numerical test on the simple crustal extension model with HTI symmetry provides useful insights for the imaged P-to-S (including P-to-SV and P-to-SH) conversions in the stacked and back-azimuth domains at the lithospheric discontinuities, with or without appropriate treatments of the seismic anisotropy. The synthetic example on the subduction model with strong heterogeneities and spatially varied TI symmetries reveals the necessity to apply passive-source anisotropic RTM to effectively characterize the boundaries and the shape of the subducted slab. With constantly emerging deployments of regionally extensive seismic arrays and increasing efforts for 3-D regionally anisotropic model building, the proposed wave-equation based approach will play an important role in 3-D lithospheric imaging.

Acknowledgments

This work is supported by the National Natural Science Foundation of China (42074157 & 41674117) and the National Key R&D Program of China (2017YFB0202903). We appreciate Mei Xue and Youqiang Yu for their useful suggestions, and Chenlong Wang for provid-

ing the original 2-D passive source RTM code. The first author thanks Tengfei Wang and Sihai Wu for the help in GPU-based parallel computing. All the data is generated by the methods presented in the paper which can be easily reproduced with the given model parameters. The codes of low rank approximation for wave mode decomposition are available in Madagascar open-source software package (http://www.ahay.org).

References

Anderson, D. L., & Regan, J. (1983). Uppermantle anisotropy and the oceanic lithosphere. *Geophysical Research Letters*, *10*(9), 841–844.

Auld, B. A. (1973). *Acoustic fields and waves in solids* (Vol. I). Wiley, New York.

Backus, G. E. (1962). Long-wave elastic anisotropy produced by horizontal layering. *Journal of Geophysical Research*, *67*(11), 4427–4440.

Baysal, E., Kosloff, D. D., & Sherwood, J. W. (1983). Reverse time migration. *Geophysics*, *48*(11), 1514–1524.

Becker, T. W., Chevrot, S., Schulte-Pelkum, V., & Blackman, D. K. (2006). Statistical properties of seismic anisotropy predicted by upper mantle geodynamic models. *Journal of Geophysical Research: Solid Earth*, *111*(B8).

Beller, S., & Chevrot, S. (2020). Probing depth and lateral variations of upper-mantle seismic anisotropy from full-waveform inversion of teleseismic body-waves. *Geophysical Journal International*, *222*(1), 352–387.

Beylkin, G. (1985). Imaging of discontinuities in the inverse scattering problem by inversion of a causal generalized radon transform. *Journal of Mathematical Physics*, *26*(1), 99–108.

Bostock, M., & Rondenay, S. (1999). Migration of scattered teleseismic body waves. *Geophysical journal international*, *137*(3), 732–746.

Brytik, V., De Hoop, M. V., & Van Der Hilst, R. D. (2012). Elastic-wave inverse scattering based on reverse time migration with active and passive source reflection data. *Inverse problems and applications: Inside out II*, *60*, 411.

Chang, S.-J., Ferreira, A. M., Ritsema, J., van Heijst, H. J., & Woodhouse, J. H. (2015). Joint inversion for global isotropic and radially anisotropic mantle structure including crustal thickness perturbations. *Journal of Geophysical Research: Solid Earth*, *120*(6), 4278–4300.

Chen, L., Wen, L., & Zheng, T. (2005). A wave equation migration method for receiver function imaging: 1. theory. *Journal of Geophysical Research: Solid Earth*, *110*(B11).

Chen, M., Niu, F., Liu, Q., Tromp, J., & Zheng, X. (2015). Multiparameter adjoint tomography of the crust and upper mantle beneath east asia: 1. model construction and comparisons. *Journal of Geophysical Research: Solid Earth*, *120*(3), 1762–1786.

Cheng, C., Bodin, T., & Allen, R. M. (2016). Three-dimensional pre-stack depth migration of receiver functions with the fast marching method: a kirchhoff approach. *Geophysical Journal International*, *205*(2), 819–829.

Cheng, J., & Fomel, S. (2014). Fast algorithms for elastic-wave-mode separation and vector decomposition using low-rank approximation for anisotropic media. *Geophysics*, *79*(4), C97–C110.

Cheng, J., & Kang, W. (2014). Simulating propagation of separated wave modes in general anisotropic media, part i: qp-wave propagators. *Geophysics*, *79*(1), C1–C18.

Cheng, J., & Kang, W. (2016). Simulating propagation of separated wave modes in general anisotropic media, part ii: qs-wave propagators. *Geophysics*, *81*(2), C39–C52.

Christensen, N. I. (1966). Shear wave velocities in metamorphic rocks at pressures to 10 kilobars. *Journal of Geophysical Research*, *71*(14), 3549–3556.

Crampin, S. (1984). Effective anisotropic elastic constants for wave propagation through cracked solids. *Geophysical Journal International*, *76*(1), 135–145.

Crampin, S. (1989). Suggestions for a consistent terminology for seismic anisotropy. *Geophysical Prospecting*, *37*(7), 753–770.

Crampin, S., & Yedlin, M. (1981). Shear-wave singularities of wave propagation in anisotropic media. *Journal of Geophysics*, *49*, 43-46.

Dellinger, J. (1991). *Anisotropic seismic wave propagation*. Ph.D. thesis, Stanford University.

Dueker, K. G., & Sheehan, A. F. (1997). Mantle discontinuity structure from midpoint stacks of converted p to s waves across the yellowstone hotspot track. *Journal of Geophysical Research: Solid Earth*, *102*(B4), 8313–8327.

Dziewonski, A. M., & Anderson, D. L. (1981). Preliminary reference earth model. *Physics of the Earth and Planetary Interiors*, *25*(4), 297-356.

Eberhart-Phillips, D., & Reyners, M. (2009). Three-dimensional distribution of seismic anisotropy in the hikurangi subduction zone beneath the central north island, new zealand. *Journal of Geophysical Research: Solid Earth*, *114*(B6).

Eckhardt, C., & Rabbel, W. (2011). Preceiver functions of anisotropic continental crust: a hierarchic catalogue of crustal models and azimuthal waveform patterns. *Geophysical Jour-*

nal International(187), 439-479.

Fouch, M. J., & Rondenay, S. (2006). Seismic anisotropy beneath stable continental interiors. *Physics of the Earth and Planetary Interiors*, *158*(2-4), 292-320.

Gao, S. S., & Liu, K. H. (2014). Mantle transition zone discontinuities beneath the contiguous united states. *Journal of Geophysical Research: Solid Earth*, *119*(8), 6452–6468.

Godfrey, N. J., Christensen, N. I., & Okaya, D. A. (2000). Anisotropy of schists: Contribution of crustal anisotropy to active source seismic experiments and shear wave splitting observations. *Journal of Geophysical Research: Solid Earth*, *105*(B12), 27991–28007.

Huang, Z., Zhao, D., & Wang, L. (2011). Seismic heterogeneity and anisotropy of the honshu arc from the japan trench to the japan sea. *Geophysical Journal International*, *184*(3), 1428–1444.

Jiang, X., Zhu, L., Hu, S., & Rong, H. (2019). Three-dimensional reverse-time migration of teleseismic receiver functions using the phase-shift-plus-interpolation method. *Journal of Geophysical Research: Solid Earth*, *217*(1), 1047–1057.

Jones, K., Warner, M., & Brittan, J. (1999). Anisotropy in multi-offset deep-crustal seismic experiments. *Geophysical Journal International*, *138*(2), 300–318.

Kaneshima, S., Ando, M., & Kimura, S. (1988). Evidence from shear-wave splitting for the restriction of seismic anisotropy to the upper crust. *Nature*, *335*(6191), 627.

Kosloff, D., & Baysal, E. (1982). Forward modelling by a Fourier method. *Geophysics*, *47*, 1402-1412.

Langston, C. A. (1979). Structure under mount rainier, washington, inferred from teleseismic body waves. *Journal of Geophysical Research: Solid Earth*, *84*(B9), 4749–4762.

Laske, G., Masters, G., Ma, Z., & Pasyanos, M. (2013). Update on crust1.0 – a 1-degree global model of earths crust. *In Geophysical Research Abstracts*, 15.

Lebedev, S., & Hilst, R. D. V. D. (2008). Global upper-mantle tomography with the automated multimode inversion of surface and s-wave forms. *Geophysical Journal International*, *173*, 505-518.

Levander, A., Niu, F., Symes, W. W., & Nolet, G. (2005). Imaging teleseismic p to s scattered waves using the kirchhoff integral. *Geophysical Monograph-American Geophysical Union*, *157*, 149.

Levin, V., & Park, J. (1997). Crustal anisotropy in the ural mountains foredeep from teleseismic receiver functions. *Geophysical Research Letters*, *24*(11), 1283–1286.

Levin, V., & Park, J. (1998). P-sh conversions in layered media with hexagonally symmetric

anisotropy: a cookbook. *Pure and Applied Geophysics*, *151*, 669–697.

Li, J., Shen, Y., & Zhang, W. (2018). Three-dimensional passive-source reverse-time migration of converted waves: The method. *Journal of Geophysical Research: Solid Earth*, *123*(2), 1419–1434.

Liu, H., & Niu, F. (2012). Estimating crustal seismic anisotropy with a joint analysis of radial and transverse receiver function data. *Geophysical Journal International*, *188*(1), 144–164.

Long, M. D., & Wirth, E. A. (2013). Mantle flow in subduction systems: The mantle wedge flow field and implications for wedge processes. *Journal of Geophysical Research: Solid Earth*, *118*(2), 583–606.

Mainprice, D., Tommasi, A., Couvy, H., Cordier, P., & Frost, D. (2005). Pressure sensitivity of olivine slip systems and seismic anisotropy of earth's upper mantle. *Nature*, *433*(7027), 731-3.

McNamara, D. E., & Owens, T. J. (1993). Azimuthal shear wave velocity anisotropy in the basin and range province using moho ps converted phases. *Journal of Geophysical Research: Solid Earth*, *98*(B7), 12003–12017.

Nishizawa, O. (1982). Seismic velocity anisotropy in a medium containing oriented cracks. *Journal of Physics of the Earth*, *30*(4), 331–347.

Pasyanos, M. E., Masters, T. G., Laske, G., & Ma, Z. (2014). Litho1.0: An updated crust and lithospheric model of the earth. *Journal of Geophysical Research: Solid Earth*, *119*(3), 2153-2173.

Poppeliers, C., & Pavlis, G. L. (2003). Three-dimensional, prestack, plane wave migration of teleseismic p-to-s converted phases: 1. theory. *Journal of Geophysical Research: Solid Earth*, *108*(B2).

Revenaugh, J. (1995). A scattered-wave image of subduction beneath the transverse ranges. *Science*, *268*(5219), 1888–1892.

Rondenay, S. (2009). Upper mantle imaging with array recordings of converted and scattered teleseismic waves. *Surveys in Geophysics*, *30*(4-5), 377–405.

Rumpker, G., Kaviani, A., & Latifi, K. (2014). Ps-splitting analysis for multilayered anisotropic media by azimuthal stacking and layer stripping. *Geophysical Journal International*(199), 146-163.

Ryberg, T., & Weber, M. (2000). Receiver function arrays: a reflection seismic approach. *Geophysical Journal International*, *141*(1), 1–11.

Saenger, E. H., & Bohlen, T. (2004). Finite-difference modeling of viscoelastic and anisotropic wave propagation using the rotated staggered grid. *Geophysics*, *69*(2), 583-591.

Savage, M. (1999). Seismic anisotropy and mantle deformation: what have we learned from shear wave splitting? *Reviews of Geophysics*, *37*(1), 65–106.

Schaeffer, A. J., Lebedev, S., & Becker, T. W. (2016). Azimuthal seismic anisotropy in the earth's upper mantle and the thickness of tectonic plates. *Geophysical Journal International*, *207*(8), 901-933.

Shang, X., de Hoop, M. V., & van der Hilst, R. D. (2012). Beyond receiver functions: Passive source reverse time migration and inverse scattering of converted waves. *Geophysical Research Letters*, *39*(15).

Tarantola, A. (1984). Inversion of seismic reflection data in the acoustic approximation. *Geophysics*, *49*, 1259-1266.

Thomsen, L. (1986). Weak elastic anisotropy. *Geophysics*, *51*(10), 1954–1966.

Tsvankin, I. (1997). Reflection moveout and parameter estimation for horizontal transverse isotropy. *Geophysics*, *62*(2), 614–629.

Vinnik, L. (1977). Detection of waves converted from p to sv in the mantle. *Physics of the Earth and Planetary Interiors*, *15*(1), 39–45.

Wang, C., Cheng, J., & Arntsen, B. (2016). Scalar and vector imaging based on wave mode decoupling for elastic reverse time migration in isotropic and transversely isotropic media. *Geophysics*, *81*(5), S383–S398.

Wang, J., & Zhao, D. (2012). P wave anisotropic tomography of the nankai subduction zone in southwest japan. *Geochemistry, Geophysics, Geosystems*, *13*(5).

Xie, J., Ritzwoller, M. H., Shen, W., & Wang, W. (2017). Crustal anisotropy across eastern tibet and surroundings modeled as a depth-dependent tilted hexagonally symmetric medium. *Geophysical Journal International*, *209*(1), 466–491.

Yan, J., & Sava, P. (2009). Elastic wave-mode separation for VTI media. *Geophysics*, *74*(5), WB19–WB32.

Yuan, K., & Beghein, C. (2013). Seismic anisotropy changes across upper mantle phase transitions. *Earth and Planetary Science Letters*, *374*, 132-144.

Zhang, Q., & McMechan, G. A. (2010). 2D and 3D elastic wavefield vector decomposition in the wavenumber domain for VTI media. *Geophysics*, *75*(3), D13-D26.

Zhao, D., Sheng, Y., & Xin, L. (2016). Seismic anisotropy tomography: New insight into

subduction dynamics. *Gondwana Research*, *33*, 24-43.

Zhu, H., Stern, R. J., & Yang, J. (2020). Seismic evidence for subduction-induced mantle flows underneath middle america. *Nature Communications*, *11*(1), 1–12.

Zhu, L. (2000). Crustal structure across the san andreas fault, southern california from teleseismic converted waves. *Earth and Planetary Science Letters*, *179*(1), 183–190.

Zou, P., & Cheng, J. (2018). Pseudo-spectral method using rotated staggered grid for elastic wave propagation in 3d arbitrary anisotropic media. *Geophysical Prospecting*, *66*, 47-61.

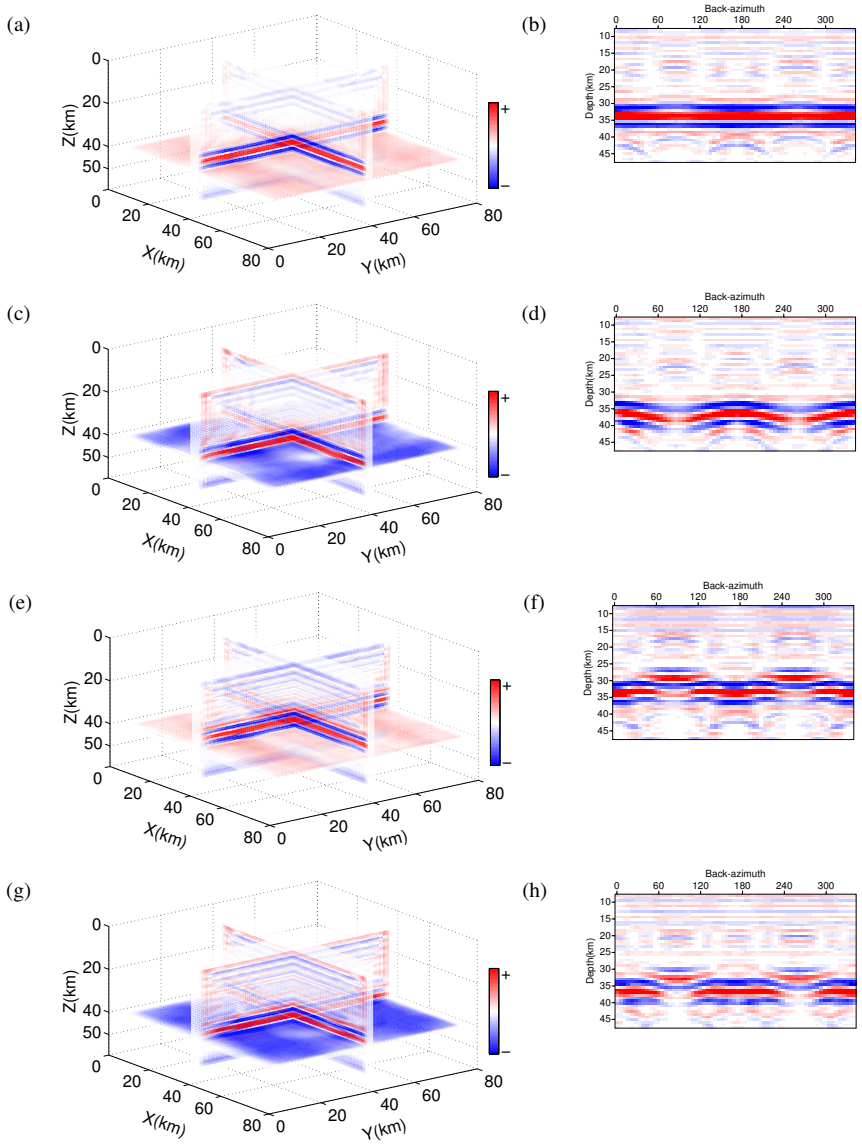

Figure 4: 3-D anisotropic RTM images (left) and common image gathers (right) obtained with (a, b) the true anisotropic model, and inaccurate anisotropic models by setting (c, d) $\epsilon = 0$, (e, f) $\gamma = 0$, (g, h) $\epsilon = 0, \gamma = 0$ and $\delta = 0$. The true depth of the Moho is $33km$ and the horizontal slices in the 3-D RTM images are shown at the depth of $40km$.

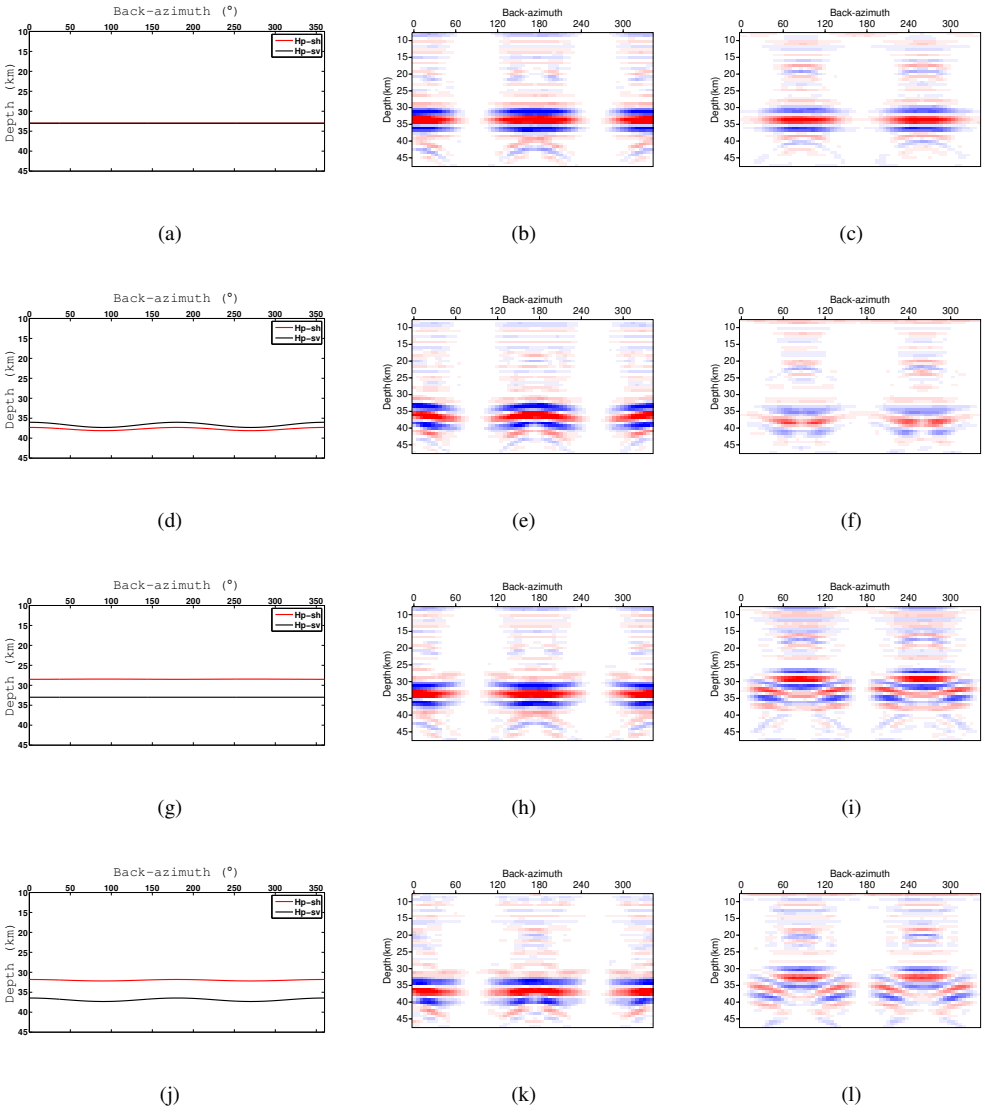

Figure 5: Estimated imaging depths using the phase velocity formulations (left) and the common image gathers for the decoupled P-SV (middle) and P-SH (right) conversions with different migration velocity models: (a, b, c) true anisotropic model; (d, e, f) inaccurate anisotropic model by setting $\epsilon = 0$; (g, h, i) inaccurate anisotropic model by setting $\gamma = 0$; and (j, k, l) isotropic model by setting $\epsilon = 0, \gamma = 0$ and $\delta = 0$.

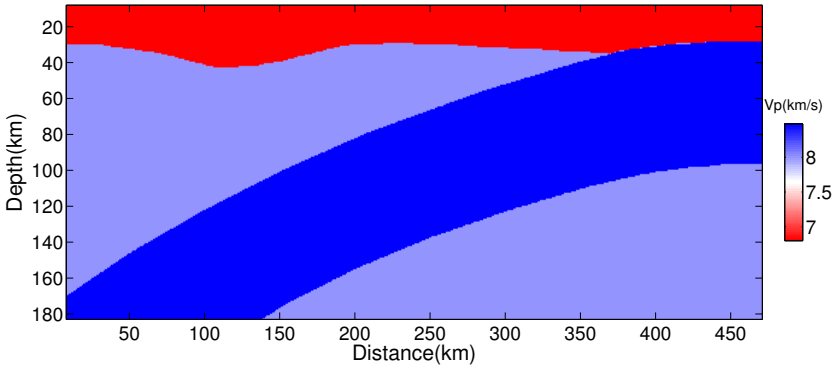

(a)

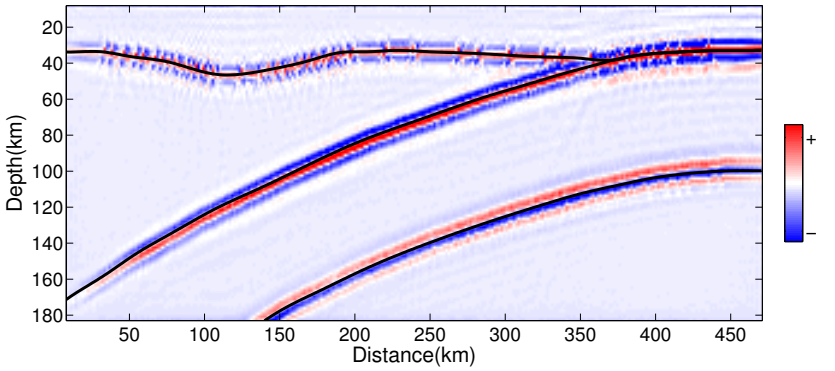

(b)

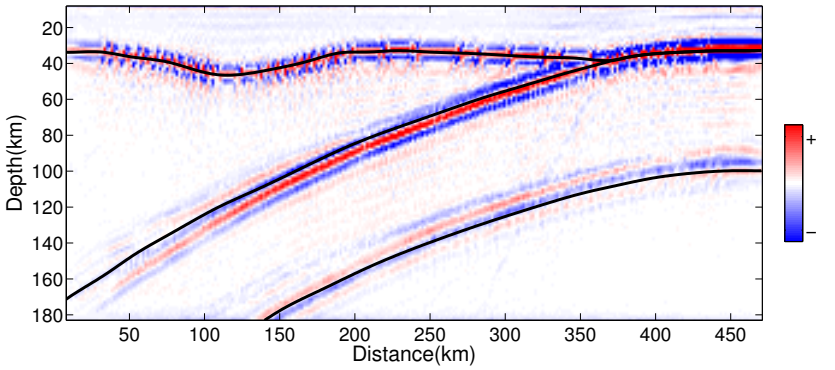

(c)

Figure 6: Image result of one vertical slice perpendicular to the strike of the subduction zone: (a) is the P-wave velocity model of the simplified subduction zone; (b) is the 3-D passive-source RTM image result of the subduction zone structure considering all the anisotropic effects. (c) is the image result ignoring all the anisotropic parameters. The thin black lines in (b) and (c) depict the true elastic discontinuity interfaces.

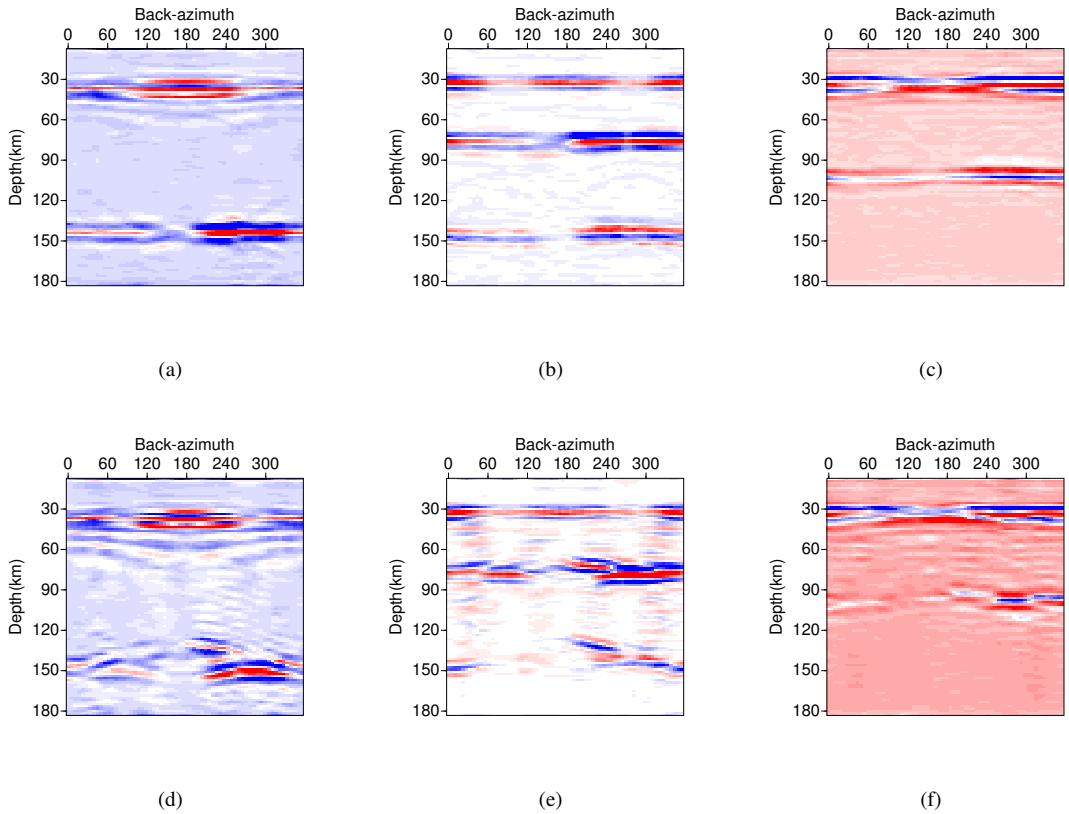

Figure 7: The common image gathers at $72km$(a,d), $240km$(b,e) and $420km$(c,f), respectively. (a, b, c) are the result of 3-D passive-source anisotropic RTM and (d, e, f) are the result of 3-D passive-source isotropic RTM.